CFDST sections with square stainless steel outer tubes under axial compression: Experimental investigation, numerical modelling and design

Fangying Wang[a]*, Ben Young[b], Leroy Gardner[c]

[a] *Department of Civil Engineering, The University of Hong Kong, Pokfulam Road, Hong Kong, China.*
[b] *Department of Civil and Environmental Engineering, The Hong Kong Polytechnic University, Hong Kong, China. (Formerly, Department of Civil Engineering, The University of Hong Kong, Pokfulam Road, Hong Kong, China.)*
[c] *Department of Civil and Environmental Engineering, Imperial College London, London, UK*

*corresponding author:christine.wang@connect.hku.hk

Keywords: Composite structures; CFDST; Experiments; Numerical modelling; Stainless steel; Tubular structures.

Abstract

The use of concrete-filled double skin tubular (CFDST) cross-sections for compression members has become increasingly popular in construction. A recently proposed innovative form of CFDST cross-section, ultilising stainless steel for the outer tube, offers the combined advantages of the composite action seen in CFDST member alongside the durability and ductility associated with stainless steel. CFDST sections with stainless steel outer tubes, for which there are currently little experimental data, are the focus of the present study. A comprehensive experimental and numerical investigation into the compressive behaviour of CFDST sections with square stainless steel outer tubes is presented in this paper. A total of 19 specimens was tested under uniform axial compression, and the test observations are fully reported. The ultimate loads, load-displacement curves and failure modes from the tests were used for the validation of finite element (FE) models. Parametric finite element analyses were then performed. The combined set of experimentally and numerically derived data was employed to assess the applicability of the existing European, Australian and American design

provisions for composite carbon steel members to the design of the studied CFDST cross-sections. Overall, the existing design rules are shown to provide generally safe-sided (less so for the higher concrete grades) but rather scattered capacity predictions. Modifications to the current design codes are also considered—a higher buckling coefficient k of 10.67 to consider the beneficial restraining effect of the concrete on the local buckling of the stainless steel outer tubes, as well as a reduction factor η to reflect the reduced relative effectiveness of higher concrete grades. Overall, the comparisons demonstrated that improved accuracy and consistency were achieved when the modified design rules were applied.

1. Introduction

Concrete-filled double skin tubular (CFDST) sections consist of two metal tubes—an outer and inner tube—with concrete infilled between the tubes. CFDST sections, which fall into the general category of concrete-filled steel tubular (CFST) sections, have been gaining increasing attention in modern construction practice as they offer an excellent combination of high strength, stiffness and ductility [1]. CFDST sections share the constructability benefits of CFST sections, with the steel tubes acting as permanent formwork, but will typically be lighter owing to the absence of the inner core of concrete. CFDST sections also possess superior fire resistance to single skin CFST sections because of the thermally protected inner tube [2].

The idea of using double skin tubular sections originated in Britain, where a deep-water vessel was constructed using double cylindrical shells filled with resin [3]. In the late 1990s, CFDST members were investigated for their potential applications in offshore construction [4] and bridge piers [5]. A prominent example of the use of CFDST columns in a transmission tower is described in [6]. In the last two decades, CFDST members have generated substantial interest among researchers, and a number of laboratory testing and numerical modelling programmes have been undertaken to examine their structural performance. CFDST cross-sectional configurations are diverse, and those with CHS outer and inner tubes have been the most extensively studied [7, 8]. Research into CFDST sections with SHS outer tubes and CHS inner tubes is rather limited and has mainly focussed on carbon steel members, including investigations of cross-sectional capacity [9,10], cyclic performance [11], as well as fire resistance [1]. One of the notable conclusions drawn from these investigations is that the cross-sectional slenderness and concrete grade have a great influence on the ultimate capacity and ductility of the CFDST members.

Stainless steel members have been utilised in construction increasingly over the past few decades for their unique combination of mechanical properties and corrosion resistance [12]. However, the high tonnage price of stainless steel, typically 2-5 times those of carbon steel, is a disincentive for more widespread utilisation in the industry. The nonlinear material stress–strain response typically observed for structural stainless steel alters the structural performance of bare stainless steel structural tubular cross-sections from that of carbon steel cross-sections [12]. Particularly, stocky cross-sections exhibit increased load-bearing capacities beyond the plastic resistance and higher deformation capacities; this is attributed to the substantial strain hardening of the stainless steel material. The axial compressive behaviour of square and rectangular stainless steel CFST sections has also been recently explored by [13–18]; the significant influence of the slenderness of the metal tube on the load-bearing capacity and ductility was highlighted in these studies. Uy et al. [13] documented a rather more rounded and ductile load-deformation response of stainless steel CFST stub columns compared to that of carbon steel CFST stub columns. A limited number of tests has been performed in recent years on CFDST sections utilising stainless steel for the outer tubes [7,8,19,20]. Comparisons were made to assess the applicability of existing design rules, and the resistance predictions were found to be rather scattered. With the aim of exploiting the most favourable properties of the constituent materials in CFDST columns to the greatest possible extent, a novel type of CFDST section is proposed in this study, employing a high strength steel circular hollow section (CHS) for the inner tube and a stainless steel square hollow section (SHS) for the outer tube. The interaction between the concrete infill and the metal tubes leads to efficient utilisation of the different materials by confining the concrete and delaying local buckling in the metal tubes, while the presence of the high strength steel inner tube allows the thickness of the stainless steel outer tube to be reduced, thus improving the cost-effectiveness of the system. To date, there have been no experimental or numerical investigations into the axial compressive behaviour of CFDST sections comprising stainless steel SHS outer tubes and high strength steel CHS inner tubes, and this is therefore the focus of the present study.

This paper first presents a comprehensive test programme to investigate the axial compressive performance of the examined CFDST sections. A subsequent finite element (FE) validation study is then presented, followed by parametric analyses performed over a wide range of cross-section slendernesses and concrete strengths. The full set of experimentally and numerically derived data are then employed to evaluate the applicability of the current design provisions given in the European Code EN 1994-1-1 (EC4) [21], Australian Standard AS5100 [22] and American Specifications AISC 360 [23] and ACI 318 [24] to the design of the studied CFDST cross-sections. Modifications to the design treatment in relation to the effective areas of the outer tubes to account for outward only local buckling and the effective compressive strength of the concrete are also considered.

2. Experimental investigation

2.1 General

A typical CFDST section with a high strength steel CHS as the inner tube and a stainless steel SHS as the outer tube is presented in Fig. 1. The stainless steel grade employed in the present study was austenitic grade EN 1.4062 [25]. Two cross-sections, SHS 120×120×6 mm (depth × width × thickness) and SHS 150×150×3, were adopted as the outer tubes. Three cross-sections were chosen for the high strength steel inner tubes— hot-rolled CHS 22×4 mm (diameter × thickness) and CHS 32×6 profiles and a cold-formed CHS 89×4. The nominal stub column length (L) was chosen to be 2.5 times the nominal cross-section depth, which was deemed appropriately short to prevent global buckling, yet adequately long to avoid end effects [8,14,18,20,26].

The CFDST specimens were prepared by first precisely locating the inner tubes and outer tubes concentrically, and then welding steel strips (10 mm deep and 2 mm thick) to the tubes near both ends of the stub columns to fix their relative positions, as detailed in Fig. 2. Together, the outer and inner tubes were wire cut flat and square before casting the concrete. The concrete was compacted using a poker vibrator to reduce the volume of air voids. Strain visualisation grids with a size of 15 mm × 15 mm were painted onto the specimen surfaces. Geometric measurements were carefully taken, and the average measured values are presented in Table 1, where L is the member length, B, D and t are the width, depth and thickness for the SHS and D and t are the diameter and thickness for the CHS. The subscripts o and i are used to differentiate between the outer and inner tubes; r_{int} and r_{ext} denote the internal and external corner radii of the outer tubes and A_i, A_o and A_c correspond to the calculated cross-sectional areas of the inner tube, outer tube and sandwiched concrete.

A labelling system for the studied CFDST specimens was designed so as to identify the CFDST cross-section constituents directly. For example, AS120×6-HC22×4-C120 defines a CFDST specimen with an AS120×6 (D_o×t_o) outer tube, with the letter “A” standing for austenitic stainless steel and “S” representing an SHS, and an HC22×4 (D_i×t_i) inner tube, with “H” standing for high strength steel and “C” representing a CHS. The letter “C” after the second hyphen denotes concrete infill, followed by the nominal concrete grade of C120. A label with a suffix “R” represents a repeat specimen.

2.2 Material testing

Longitudinal tensile coupon tests were carried out to obtain the material stress–strain properties of the metal tubes. Since cold-formed metal tubes undergo strength enhancement due to cold-working during production, which is particularly pronounced in the corner areas of sections, coupons were extracted from both the corner and flat regions of the SHS outer tubes, as illustrated in Fig. 3(a). For the cold-formed CHS inner tubes, a curved coupon was extracted from the quarter position around the cross-section relative to the weld, whereas for the seamless hot-rolled inner tube, a coupon was extracted from a random location within the cross-section, as shown in Fig. 3(b). Each tensile coupon extracted from the CHS inner tubes was labelled by its cross-section identifier, while the flat (F) and corner (C) coupons extracted from the SHS outer tubes were differentiated by their cross-section identifier and a suffix (either F or C) designating their origin. Each flat coupon was prepared in conformance with ASTM E8M-15 [27], with a 12 mm parallel width and a 50 mm gauge length, while each corner or curved coupon had a parallel width of 4 mm and a gauge length of 25 mm. For the corner and curved coupons, two 10.5 mm diameter holes were drilled and reamed at 17 mm from each end. The flat coupons were gripped using a set of end-clamps, while a pair of steel rods was inserted into the drilled holes of the corner coupons, through which the tensile force was applied, as shown in Fig. 4. A contact extensometer was attached to the coupons and a strain gauge was affixed to each side of the coupons at mid-length. All the longitudinal tensile coupon tests were displacement controlled and conducted in an MTS 50 kN testing machine. A constant displacement rate of 0.05 mm/min was used in the elastic range of the stress–strain curves, whereas a higher rate of 0.4 mm/min was used in the inelastic range; in the post-ultimate range, a rate of 0.8 mm/min was adopted, as recommended in Huang and Young [28].

The static 0.2% proof stress $\sigma_{0.2}$, static ultimate tensile stress σ_u, Young's modulus E, elongation at fracture ε_f, and compound Ramberg-Osgood (R-O) material model strain hardening exponents n and m [29–32], as determined from the coupon tests are summarised in Table 2. The process of cold-forming was shown to result in a moderate enhancement in both $\sigma_{0.2}$ and σ_u in the corner regions, though this is accompanied by a reduction in ductility. Comparisons of the full stress–strain curves in Fig. 5 reveal that the high strength steel inner tubes possess higher 0.2% proof stresses and ultimate strengths, but less pronounced strain hardening and much lower ductility than the stainless steel outer tubes.

Concrete cylinder tests were performed to obtain the material properties of the concrete. Three concrete grades—C40, C80, and C120 MPa—were produced in the laboratory using commercially available materials. Their mix proportions are presented in Table 3. For each batch of concrete, cylinders were cast and air-cured together with the CFDST test specimens. Two concrete cylinders were utilised to obtain the average 28-day concrete strengths and the remainder were tested on the days of the respective CFDST specimen tests. Table 4 summarises the mean measured strengths and the test number for each concrete grade.

2.3 Axial compressive testing

A total of 19 CFDST specimens, including four repeated to assess the variability of the results, was tested under uniform axial compression in an INSTRON 5000 kN capacity servo-controlled hydraulic machine. A typical CFDST stub column test setup is illustrated in Fig. 6(a). The ends of each specimen were clamped using a steel reinforcing frame with a 25 mm height to avoid premature end failure, as shown in Fig. 6(b). A thin layer (< 1 mm) of plaster was applied to the top surface of the cast CFDST specimens to eliminate any gaps arising due to concrete shrinkage. The plaster was then left to harden under an approximately 2 kN applied load. This ensured uniform loading on the top surface of the specimens throughout the tests. Three 50 mm range displacement transducers (LVDTs) were placed between the testing machine platens to measure the axial shortening. The strain development histories and plate deformations were also monitored through four pairs of longitudinal and transverse strain gauges affixed at the centre of the flat face and at the corner of the 1/3 and 2/3 points along the stub column heights. The LVDT readings contain both the end shortening of the stub column specimens and the deformation of the end platens of the testing machine. The true axial deformation of the stub column specimens was thus obtained by eliminating the deformation of the end platens of the testing machine from the LVDT measurements based on the strain gauge readings [33,34]. The load–true average axial strain curves were derived by assuming that the end platen deformation was proportional to the applied load and shifting the load–axial strain curve derived from the LVDTs such that its initial slope matched that obtained from the strain gauges. The load versus true axial deformation curves are employed in Section 3 for the validation of the FE models. A constant 0.4 mm/min displacement rate was used to drive the bottom end platen of the testing machine upwards in order to apply the load to the stub columns [8,20].

2.4 Test results

The load (P) versus average axial strain (ε) curves for all the stub column specimens are plotted in Fig. 7, where P is the applied load recorded by the load actuator and ε is the measured average axial strain, defined as the average axial shortening (Δ), calculated from the LVDT readings, divided by the original measured specimen length (L). The ultimate experimental loads (P_{exp}) are presented in Table 1. The ultimate strength of test specimen AS150×3-HC89×4-C80 appeared to be slightly lower than expected. This may have stemmed from the presence of excess air voids in the concrete, that were not eliminated during the specimen preparation. The P–ε curves for two stocky specimens did not reach a peak value despite large plastic deformations; these specimens are marked with an asterisk in Table 1. For these specimens, the ultimate load was defined as the load at which the tangential stiffness of the load-average axial strain curve reached 1% of its initial stiffness, taken as the average slope in the initial linear portion of the curve. This approach was proposed by dos Santos et al. [35] and has been employed for the definition of the ultimate loads of CFDST stub columns in [8]. From the load-deformation curves, it was observed that CFDST columns using stainless steel for the outer tubes generally exhibited a rather more rounded and ductile response than that seen from existing tests on carbon steel CFDST stub columns [9,10]; this mirrors the findings for concrete-filled stainless steel tubular members in [13]. This behaviour is directly linked to the rounded stress–strain response and substantial strain hardening that characterises stainless steel alloys.

The ductility of the CFDST stub columns was assessed through the ductility index (DI) [8,18,20], which is defined as the ratio of the axial displacement when the load dropped to 85% of the ultimate load ($\Delta_{85\%}$) to the axial displacement at the ultimate load (Δ_u), as presented in Table 1. In cases where the load did not drop to $0.85P_{exp}$, the DI values was calculated on the basis of the maximum obtained displacement, as indicated by a '>' symbol in Table 1. A high

DI value indicates an ability to maintain at least 85% of P_{exp} with a considerable associated deformation. Overall, it is evident that all the tested stub columns generally possessed high ductility, and that higher concrete strengths resulted in increased compressive resistance but lower ductility. It can also be seen that the *DI* values for the specimens with the highest strength inner tubes (HC89×4) were generally lower than their counterparts with lower strength inner tubes (HC22×4 and HC32×6).

The failure modes of the CFDST stub columns featured local buckling of the metal tubes and crushing of the infill concrete. The SHS outer tube only buckled outwards, as shown in Fig. 8(a) and (b). This is attributed to the presence of the concrete, which inhibits inward deformations. This outward only buckling mode is similar to that described in Refs [9–11] for carbon steel CFDST stub columns. No apparent local buckling was observed for the inner tubes in this study. Concrete failure was observed in the regions where local buckling of the outer tubes occurred, and the concrete crushing may indeed have triggered the local buckling failures.

3. Numerical modelling

3.1 Finite element models

A numerical modelling study employing the general-purpose FE analysis package ABAQUS [36], was carried out in conjunction with the laboratory testing program. The experimental results were first successfully replicated by the FE models. Parametric analyses were subsequently performed over a wide range of cross-section slendernesses and concrete grades.

An FE model of each test specimen presented in Section 2 was established based on the measured geometries using S4R shell elements [36] for the metal tubes and C3D8R solid elements for the sandwiched concrete, in line with previous FE modelling of concrete-filled tubular members [8,37–40]. In the tests, the geometry, loading and failure modes were doubly symmetric. Hence, to enhance computational efficiency, only one-quarter of the cross-sections and half of the member lengths were modelled, with suitable boundary conditions assigned to the planes of symmetry, as depicted in Fig. 9. Following a prior mesh sensitivity study, uniform mesh seed sizes of min(D_o/30, πD_i/60) were chosen for the CFDST cross-sections, while 30 seeds were applied in the longitudinal direction; these mesh settings were found to produce accurate yet computationally efficient results.

The measured material properties were incorporated into the respective FE simulations for validation purposes. For the metal tubes, the measured engineering stress–strain curves, characterised by at least 100 points from the tensile coupon test curves, were converted into true stress–true plastic strain curves, and input into ABAQUS. For the austenitic stainless steel SHS, the coupon tests revealed that the yield strength of the corner material was about 20% higher, on average, than that of the flat material. Allowance for this was therefore made in the developed FE models by assigning the corner material properties to the curved corner regions of the SHS plus an extended region equal to two times the section thickness into the adjacent flat region, following the recommendations of [41]. For the sandwiched concrete, the Abaqus concrete damage plasticity (CDP) model [36] was adopted, with the confined concrete stress-strain response, based on that proposed by Tao et al. [37] for CFST stub columns, as modified by Wang et al. [8] for application to CFDST stub columns with CHS outer tubes. The modifications were concerned primarily with the confinement factor (ξ_c), defined in Eq. (1),

$$\xi_c = \frac{A_o \sigma_{0.2,o}}{A_{ce} f_c} \tag{1}$$

where A_{ce} is an equivalent cross-sectional area of concrete, defined as the full area enclosed by the outer tube, as given by Eq. (2).

$$A_{ce} = (D_o - 2t_o)^2 - (4-\pi) r_{int,o}{}^2 \tag{2}$$

The Poisson's ratio of the concrete and modulus of elasticity E_c were taken respectively as 0.2 and $4733\sqrt{f_c}$, according to the recommendations of ACI 318 [24]. For the tensile stress-strain properties of the concrete, a linear response was assumed before reaching the tensile strength (taken as 0.1 f_c) ; the subsequent post-peak behaviour was characterised through fracture energy (G_F) [36, 37].

The interaction between the outer and inner tubes and the concrete was simulated by surface-to-surface contact, employing "Hard contact" in the normal direction and the Coulomb friction model in the tangential direction. A friction coefficient of 0.6 was chosen for both interfaces (i.e. outer tube-concrete and inner tube-concrete) for all the FE models, though a prior parameter sensitivity study had indicated that the behaviour of the studied CFDST stub columns was relatively insensitive to the value of this parameter [42]. This is principally because the slip at the interfaces was negligible since the concrete and the metal tubes deformed simultaneously during the tests.

Initial local geometric imperfections and residual stresses are known to influence the compressive performance of bare steel members [43–46], but have been shown [37] to have no significant effect on the behaviour of concrete-filled stub columns and were thus excluded from the current FE simulations. The lack of sensitivity to imperfections is attributed to the presence of the infill concrete—in particular, the lateral pressure applied by the concrete to the steel tubes obviates the need to assign any geometry perturbation to induce local buckling while, at the same time, the support provided by the concrete lessens the susceptibility of the tubes to local instabilities. The suitability of this assumption is confirmed through the validation of the FE models.

3.2. Validation of FE models

Validation of the FE models was made with reference to the results of the 19 CFDST stub columns presented in Section 2; comparisons were made of the ultimate loads, load-displacement curves as well as failure modes. The ultimate compressive capacities obtained from the FE models normalised by the measured experimental values (P_{FE}/P_{exp}) are provided in Table 1. A mean P_{FE}/P_{exp} of 0.96 with a coefficient of variation (COV) of 0.038 was achieved, revealing that the FE ultimate strengths are generally in close agreement with those obtained from the tests. The experimental and numerical load–true average axial strain curves were also compared; a typical series of specimens with three concrete grades are displayed in Fig. 10; for the FE models, the true average axial strain was determined as the average axial shortening divided by the original length of the modelled specimen. The comparisons showed that the FE models could reproduce accurately the full loading histories of the respective stub column tests. Good agreement was also obtained for the exhibited failure modes, as shown in Fig. 8. Overall, it may be concluded that the FE models developed in this study are able to reliably replicate the structural behaviour and ultimate response observed in the experiments.

3.3 Parametric study

A parametric study was undertaken to generate additional FE results for a range of key input parameters. The measured material properties of the austenitic stainless steel section AS120×3 and the high strength steel section HC32×6 were incorporated into all the modelled outer tubes and inner tubes, respectively. Concrete compressive strengths of 40, 80 and 120 MPa were used for the infilled concrete. A series of CFDST cross-sections was included in the parametric study, with the aim of covering compact, noncompact and slender sections, with reference to the classification limits for composite sections in AISC 360 [23]. The local slenderness of the outer tube was thus varied over a range of d_o/t_o values from 6 to 146, where d_o is the flat element depth of the outer tube. For the inner tubes, the local slenderness (D_i/t_i) was varied from 5 to 200. Table 5 summarises the range of the aforementioned parameters investigated in this study. All the modelled specimen lengths were set equal to $2.5D_o$, mirroring the test specimens. Overall, a total of 290 CFDST specimens was modelled in the parametric study.

4. Discussion and assessment of current design methods

4.1 General

In this section, the applicability of current codified provisions to the design of the studied CFDST cross-sections is appraised. The experimental and numerical ultimate loads are compared with the resistance predictions determined from the European Code EN 1994-1-1 (EC4) [21], the Australian Standard AS 5100 [22] and the two American Specifications—AISC 360 [23] and ACI 318 [24] for the design of composite carbon steel members. In the comparisons presented, the measured/modelled material properties and geometric dimensions of the test/FE specimens have been employed, and all partial safety factors have been taken to be equal to unity. Limitations specified in the codes on cross-sectional slenderness and material strengths are summarised in Table 6. Note that although the code limitations on the strength of concrete and steel are often exceeded, comparisons and evaluations are still presented to explore possible extension of the codes beyond their current range of applicability.

4.2 European Code EC4

The design expression for the axial compressive resistance of square or rectangular carbon steel CFST sections in EC4 [21] is a summation of the plastic resistance of the metal tubes and the concrete infill. Account is taken of the higher strength of the concrete infill as a result of the confinement provided by the outer tube, by implementing a concrete coefficient of 1.0, rather than 0.85. The analogous cross-section capacity (P_{EC4}) of a concrete-filled square or rectangular CFDST cross-section in compression is thus given by Eq. (3).

$$P_{EC4} = A_o \sigma_{0.2,o} + A_c f_c + A_i \sigma_{0.2,i} \tag{3}$$

A slenderness limit of $D_o/t_o \leq 52(235/f_y)^{0.5}$ for the outer tube of concrete-filled composite members is defined in EC4 [21]. Beyond this limit, the effects of local buckling need to be considered. A slightly modified version of this slenderness limit is employed in this study to account for the difference in Young's modulus between stainless steel and carbon steel, as given by $D_o/t_o \leq 52\sqrt{(235/\sigma_{0.2,o})(E_o/210000)}$. For CFDST sections exceeding this slenderness limit, the effective width formula set out in EN 1993-1-4 [47,48] for slender stainless steel sections, as given by Eqs (4) and (5), is used for calculating the effective area of the outer tube:

$$\rho = \frac{0.772}{\bar{\lambda}_p} - \frac{0.079}{\bar{\lambda}_p^{\ 2}} \tag{4}$$

$$\bar{\lambda}_p = \sqrt{\frac{\sigma_{0.2,o}}{\sigma_{cr}}} = \sqrt{\frac{12(1-\upsilon^2)\sigma_{0.2,o}}{k\pi^2 E_o}}\,(d_o/t_o) \tag{5}$$

where ρ is the local buckling reduction factor, $\bar{\lambda}_p$ is the local slenderness of the flat faces of the stainless steel outer tube, v is the Poisson's ratio equal to 0.3, d_o is the flat element depth of the outer tube (replaced by b_o for the flat element width), E_o is the Young's modulus of the outer tube, and k is the buckling coefficient, taken equal to 4 for plates with simply supported boundary conditions in pure compression [47].

4.3 Australian Standard AS 5100

The Australian Standard AS 5100 [22] adopts the same approach to obtain the axial compressive design strengths as EC4 [21], with the only difference being the slenderness limit. A yield slenderness limit of 40 is specified for the flat faces of the outer tube (λ_e) in AS 5100, where the local slenderness, λ_e , modified to account for the lower Young's modulus of stainless steel, is given by Eq. (6),

$$\lambda_e = \frac{d_o}{t_o}\sqrt{\frac{\sigma_{0.2,o}}{250}} \tag{6}$$

Effective areas were again used in place of the gross areas in the calculation of the design strengths of the test specimens and numerical models that exceeded this limit to account for local buckling. The effective width expressions given in AS/NZS 4673 [49] for cold-formed stainless steel tubular cross-sections, as given by Eqs (7)-(8), were adopted for the comparisons with the Australian design provisions.

$$\rho = \frac{1 - 0.22/\lambda}{\lambda} \tag{7}$$

$$\lambda = \left(\frac{1.052}{\sqrt{k}}\right)\frac{d_o}{t_o}\left(\sqrt{\frac{F_n}{E_o}}\right) \tag{8}$$

where λ is a local slenderness, F_n is the overall buckling stress of the column and requires the calculation of the tangent modulus (E_t) using an iterative design procedure, and the other symbols are as previously defined in Eq. (4). In this study, F_n is essentially equal to $\sigma_{0.2,o}$ due to the short length of the stub columns and k is again taken as 4 referring to AS/NZS 4673 [49]. Hence, the slenderness λ defined by Eq. (8) simplifies to that employed in EN 1993-1-4 [47], denoted $\overline{\lambda}_p$ and defined by Eq. (5).

4.4 American design provisions

The applicability of two American Specifications—AISC 360 [23] and ACI 318 [24] that cover concrete-filled composite members to the design of the studied CFDST stub columns is also considered herein. The AISC 360 compressive cross-section strength (P_{AISC}) of square or rectangular concrete-filled columns is presented as a function of the slenderness (compactness) of the flat faces of the steel section (d_o/t_o). The compressive cross-section strengths (P_{AISC}) of the studied CFDST stub columns are thus calculated from Eq. (9),

$$P_{AISC} = \begin{cases} A_o\sigma_{0.2,o} + 0.85A_c f_c + A_i\sigma_{0.2,i} & \text{(Compact)} \\ P_p - \dfrac{P_p - P_y}{\left(\lambda_r - \lambda_p\right)^2}\left(\lambda - \lambda_p\right)^2 + A_i\sigma_{0.2,i} & \text{(Noncompact)} \\ A_o f_{cr} + 0.7A_c f_c + A_i\,\sigma_{0.2,i} & \text{(Slender)} \end{cases} \tag{9}$$

where P_p and P_y are determined from Eq. (10) and (11) respectively, $\lambda=d_o/t_o$ is the local slenderness of the outer tube, λ_p and λ_r correspond to the limits between compact/noncompact and noncompact/slender sections, and f_{cr} is the elastic critical local buckling stress of the outer tube, given by Eq. (12).

$$P_p = A_o\sigma_{0.2,o} + 0.85A_c f_c + A_i\sigma_{0.2,i} \tag{10}$$

$$P_y = A_o\sigma_{0.2,o} + 0.7A_c f_c + A_i\sigma_{0.2,i} \tag{11}$$

$$f_{cr} = \frac{9E_o}{\left(d_o/t_o\right)^2} \tag{12}$$

It should be noted that the contribution from the inner tube is treated as an independent term, rather than a concrete dependent term as for the reinforcing bars, in the resistance function; further explanation has been provided in previous work by the authors [8,20].

The American Concrete Institute design provisions for CFST sections, as set out in ACI 318 [24] are also assessed herein. The confinement afforded to the concrete from the steel tube is not explicitly considered in ACI 318, nor is the beneficial restraining effect of the concrete on the local buckling of the outer tubes. The cross-section resistance (P_{ACI}) is thus determined from Eq. (13).

$$P_{ACI} = A_o \sigma_{0.2,o} + 0.85 A_c f_c + A_i \sigma_{0.2,i} \tag{13}$$

The gross area of the outer tube may be used in Eq. (13) provided that the tube thickness satisfies $t_o \geq D_o(\sigma_{0.2,o}/3E_o)^{0.5}$ [24]. No guidance is given in ACI 318 for sections outside this range, but in order to enable comparisons to be made, the effective width expressions for cold-formed stainless steel tubular sections given in the SEI/ASCE-8-02 [50] were utilised in the calculations. The effective areas of the stainless steel tubes were determined using the local buckling reduction factors ρ obtained from Eqs (14)-(15),

$$\rho = \frac{1 - 0.22 / \bar{\lambda}_p}{\bar{\lambda}_p} \tag{14}$$

$$\bar{\lambda}_p = \left(\frac{1.052}{\sqrt{k}}\right)\frac{d_o}{t_o}\left(\sqrt{\frac{F_n}{E_o}}\right) \tag{15}$$

where $\bar{\lambda}_p$ is the local slenderness, termed λ in SEI/ASCE-8-02 [50], F_n is the column buckling stress, calculated using an iterative tangent modulus approach, and the other symbols are as previously defined. Taking k equal to 4 according to SEI/ASCE-8-02 [50], F_n equal to $\sigma_{0.2,o}$

due to the short length of the stub columns and v=0.3, the local slenderness calculated using Eq. (15) is the same as that obtained from Eq. (5), and hence the same symbol ($\bar{\lambda}_p$) has been adopted herein.

4.5 Assessment of current design methods

Comparisons of the test and FE results with the axial compressive resistance predictions from the described design methods are shown in Figs. 11-14, where the ratio of test (or FE) strength-to-predicted strength (P_u/P_{code}) has been plotted against the corresponding normalised cross-section slenderness (λ) of the CFDST sections; a summary of the normalised cross-section slenderness measures is presented in Table 6. It can be observed that the predictions for CFDST sections falling within the slenderness limits specified in the codes and summarised in Table 7 are overly conservative for all the design methods, indicating that there is additional structural efficiency to be sought, although for some sections falling outside the specified limits, the predictions are slightly unconservative. The conservatism in the low cross-section slenderness range stems primarily from the lack of account taken for the substantial strain hardening that characterises stainless steel, as well as the higher degree of confinement afforded to the concrete infill from stocky outer tubes. Overall, mean predictions P_u/P_{code} of 1.14, 1.11, 1.28, and 1.27, with COVs of 0.211, 0.227, 0.182, and 0.173, were obtained for EC4, AS 5100, AISC 360 and ACI 318, respectively, as shown in Table 7. From the comparisons, it is concluded that the current design rules generally result in safe-sided, but rather conservative and scattered compressive strength predictions for the studied CFDST sections.

5. Modifications to design rules

5.1 Modification for high strength concrete

The accuracy in predicting the cross-section strengths for all the studied codes can be seen in Table 8 to vary with concrete grade. In general, the design methods provide rather conservative predictions for specimens with grade C40 concrete, but the conservatism reduces for those with higher concrete grades (C80 and C120), particularly for cross-sections of low slenderness. This observation mirrors previous findings for CFST sections [14–18] and CFDST sections [8,20]; to remedy this, an effective compressive strength, as defined in EN 1992-1-1 [51], is used for concrete strengths greater than 50 MPa and below 90 MPa. The effective strength is determined by multiplying the concrete strength by a reduction factor η, as given by Eq. (16). For concrete strengths beyond 90 MPa, a constant reduction factor η of 0.8, as proposed by Liew et al. [52], is employed herein to determine the effective compressive strength for sections falling within the specified code slenderness limits.

$$\eta = \begin{cases} 1.0 - \dfrac{f_c - 50}{200} & 50\text{ MPa} < f_c \leq 90\text{ MPa} \\ 0.8 & f_c > 90\text{ MPa} \end{cases} \tag{16}$$

The experimental and numerical results are compared with the modified capacity predictions in Table 8, where the average ratios of test (or FE) strength-to-predicted strength (P_u/P_{EC4*}, $P_u/P_{AS5100*}$, P_u/P_{AISC*}, and P_u/P_{ACI*}) and the corresponding COVs for each concrete grade are presented. The comparisons reveal that all the studied design methods incorporating η yield more consistent and less scattered resistance predictions across a concrete strength range from C40 to C120.

5.2 Modification to design of steel tube

The structural performance of CFST members and hollow tubular members is fundamentally different. As observed in both the experiments and FE simulations, the presence of the concrete infill alters the failure mode of the outer steel tube by restricting it from buckling inwards. It has been shown that the elastic buckling coefficient k increases from 4 for conventional (two-way) local buckling of simply-supported plates to 10.67 for outward only local buckling [53]. A modified local buckling coefficient k of 10.67, rather than 4, has therefore been employed previously by the authors [20] to reflect the restraining effect of the concrete on the local buckling of the stainless steel outer tubes. This approach is also assessed herein in the implementation of the design rules in EC4 [21], AS 5100 [22] and ACI 318 [24], taking the local buckling coefficient k as 10.67, rather than 4, in calculating the plate slenderness and hence the effective areas of the outer tubes. It is worth noting that in AISC 360 [23], the beneficial effect of the presence of the concrete infill is already included in the cross-section classification limits. Increasing the buckling coefficient k from 4 to 10.67 corresponds to an increase in buckling stress of about 2.67 times. The noncompact slenderness limit given in AISC 360 is $1.40(E/F_y)^{0.5}$ for hollow steel sections. Increasing this limit by a factor of $\sqrt{2.67}$ leads to a slenderness limit of $2.29(E/F_y)^{0.5}$. On the basis of available experimental data and the theoretical studies [54,55], a slenderness limit of $2.26(E/F_y)^{0.5}$ is adopted for concrete-filled tubes in AISC 360 [23].

The modified axial capacity predictions from EC4 [21], AS 5100 [22] and ACI 318 [24] incorporating the higher buckling coefficient k of 10.67, and the unmodified design predictions, with k=4, are compared with the test and FE ultimate strengths in Table 9 for the slender CFDST sections that fall outside their corresponding noncompact slenderness limits. The comparisons show that the mean ratios of test-to-modified design strengths ($P_{exp}/P_{code^\wedge}$) are equal to 1.02, 1.03 and 1.15, with their corresponding COVs of 0.038, 0.037 and 0.055 for EC4 [21], AS 5100 [22] and ACI 318 [24], respectively. The mean ratios of $P_{exp}/P_{code^\wedge}$ are all closer to unity and less scattered than for the case of k=4. This illustrates that the modified design rules, considering the beneficial restraining effect of the concrete on the local buckling of the stainless steel outer tubes, yield improved consistency and accuracy in the prediction of the compressive resistance of CFDST members.

Modification to the design treatment in relation to the local slenderness of the inner tube was initially attempted, conservatively assuming that the inner tube behaves similarly to a bare hollow tube, and employing the effective area of the inner tube $A_{i,eff} = A_i(90/(D_i/t_i)\times235/\sigma_{0.2,i})^{0.5}$, rather than the full area of the inner tube A_i in the design formulations. The results are presented in Table 7, showing a difference of only 2–3% for each examined design code. The insignificant influence of the local slenderness of the inner tube on the ultimate response of the studied CFDST cross-sections is also evident in Figs. 11–14, where, for a given d_o/t_o value, the discrepancy in results between the CFDST stub columns with varying D_i/t_i values is minimal. Therefore, to retain the simplicity of the design formulations, modifications to the design treatment in relation to the local slenderness of the inner tube are not suggested herein.

6. Conclusions

A comprehensive experimental and numerical investigation into the compressive behaviour of concrete-filled double skin tubular (CFDST) sections is reported in the present paper. A total of 19 specimens were tested under uniform axial compression, and the test observations are reported. Additional data were produced using validated finite element (FE) simulations. The test and FE data were then employed to assess the applicability of the rules given in EC4 [21], AS 5100 [22], AISC 360 [23] and ACI 318 [24] for composite carbon steel members to the design of the studied CFDST cross-sections. Overall, the current design rules in EC4 [21] and AS 5100 [22] provide good average axial capacity predictions but result in a high number of strength predictions on the unsafe side, while AISC 360 [23] and ACI 318 [24] provide conservative but rather scattered predictions. Inaccuracies in the resistance predictions stemmed principally from the lack of consideration of strain hardening in the metal tubes and insufficient allowance for the strength benefits of concrete confinement applied to the concrete infill. Modifications to the current design codes were also considered— a reduction factor η to reflect the reduced relative effectiveness of using higher concrete grades and a higher buckling coefficient k of 10.67 to consider the beneficial restraining effect of the concrete on the local buckling of the stainless steel outer tubes. The comparisons demonstrated that improved accuracy and consistency is achieved using the modified design rules.

Overall, it is concluded while existing provisions are satisfactory, further improvements to the design provisions for concrete-filled double skin tubular stub columns are required, and hence further research is underway in this area.

Acknowledgements

The authors are grateful to Mr. Cheuk Him Wong for his assistance in the experimental program as part of his final year undergraduate research project at the University of Hong Kong. The authors are grateful to STALA Tube Finland for supplying the test specimens. The research work described in this paper was supported by a grant from the University of Hong Kong under the seed funding program for basic research.

References

[1] Zhao XL, Han LH. Double skin composite construction. Progress in Structural Engineering and Materials. 2006;8:93–102.

[2] Lu H, Han LH, Zhao XL. Fire performance of self-consolidating concrete filled double skin steel tubular columns: Experiments. Fire Safety Journal 2000;45(2):106–15.

[3] Montague P. A simple composite construction for cylindrical shells subjected to external pressure. Journal of Mechanical Engineering Science 1975;17(2):105–13.

[4] Wei S, Mau ST, Vipulanandan C, Mantrala SK. Performance of new sandwich tube under axial loading: experiment. Journal of Structural Engineering (ASCE) 1995;121(12):1806–14.

[5] Nakanishi K, Kitada T, Nakai H. Experimental study on ultimate strength and ductility of concrete filled steel columns under strong earthquake. Journal of Constructional Steel Research 1999;51(3):297–319.

[6] Li W, Ren QX, Han LH, Zhao XL. Behaviour of tapered concrete-filled double skin steel tubular (CFDST) stub columns. Thin-Walled Structures 2012;57:37–48.

[7] Wang F, Young B, Gardner L. Experimental investigation of concrete-filled double skin tubular stub columns with stainless steel outer tubes. Proceedings of the 8th International Conference on Steel and Aluminium Structures, Hong Kong, China, paper 118, 2016.

[8] Wang F, Young B, Gardner L. Compressive testing and numerical modelling of concrete-filled double skin CHS with austenitic stainless steel outer tubes. Thin-Walled Structures 2019;141:345–59.

[9] Zhao XL, Grzebieta R, Elchalakani M. Tests of concrete-filled double skin (SHS outer and CHS inner) composite stub columns. Advances in Steel Structures (ICASS'02) 2002:567–74.

[10] Han LH, Tao Z, Huang H, Zhao XL. Concrete-filled double skin (SHS outer and CHS inner) steel tubular beam-columns. Thin-Walled Structures 2004;42:1329–55.

[11] Han LH, Huang H, Tao Z, Zhao XL. Concrete-filled double skin steel tubular (CFDST) beam–columns subjected to cyclic bending. Engineering Structures 2006;28:1698–714.

[12] Gardner L. Stability and design of stainless steel structures – review and outlook. Thin-Walled Structures 2019;141:208–16.

[13] Uy B, Tao Z, Han LH. Behavior of short and slender concrete-filled stainless steel tubular columns. Journal of Constructional Steel Research 2011;67(3):360–78.

[14] Lam D, Gardner L. Structural design of stainless steel concrete filled columns. Journal of Constructional Steel Research 2008;64(11):1275–82.

[15] He A, Liang Y, Zhao O. Behaviour and residual compression resistances of circular high strength concrete-filled stainless steel tube (HCFSST) stub columns after exposure to fire. Engineering Structures 2020:203:109897.

[16] Young B, Ellobody E. Experimental investigation of concrete-filled cold-formed high strength stainless steel tube columns. Journal of Constructional Steel Research 2006;62(5):484–92.

[17] Lam D, Yang J, Mohammed A. (2017). Axial behavior of concrete filled lean duplex stainless steel square hollow sections. Proceedings of Eurosteel 2017—8th European Conference on Steel and Composite Structures, Copenhagen, 1(2-3), 1956–65.

[18] He A, Wang F, Zhao O. Experimental and numerical studies of concrete-filled high-chromium stainless steel tube (CFHSST) stub columns. Thin-Walled Structures 2019;144:106273.

[19] Han LH, Ren QX, Li W. Tests on stub stainless steel–concrete–carbon steel double-skin tubular (DST) columns. Journal of Constructional Steel Research 2011;67(3):437–52.

[20] Wang F, Young B, Gardner L. Experimental study of CFDST sections with stainless steel SHS and RHS outer tubes under axial compression. Journal of Structural Engineering (ASCE) 2019;145(11):04019139.

[21] EN 1994-1-1. Eurocode 4: design of composite steel and concrete structures. Part 1.1: general rules and rules for buildings. Brussels: European Committee for Standardization (CEN); 2004.

[22] Standards Australia. AS5100.6-2004 bridge design, part 6: steel and composite construction. Sydney, Australia; 2004.

[23] AISC 360. Specification for structural steel buildings. American Institute of Steel Construction, Chicago, USA; 2016.

[24] ACI 318. Building code requirements for structural concrete and commentary. Michigan, USA, Farmington Hills; 2014.

[25] BS EN 10088-1. Stainless steels-Part 1: List of stainless steels. British Standards Institution; 2014.

[26] Giakoumelis G, Lam D. Axial capacity of circular concrete-filled tube columns. Journal of Constructional Steel Research 2004;60:1049–68.

[27] American Society for Testing and Materials (ASTM). Standard test methods for tension testing of metallic materials. E8/E8M-15a, West Conshohocken, PA., USA: ASTM International; 2015.

[28] Huang Y, Young B. The art of coupon tests. Journal of Constructional Steel Research 2014;96:159–75.

[29] Mirambell E, Real E. On the calculation of deflections in structural stainless steel beams: an experimental and numerical investigation. Journal of Constructional Steel Research 2000;54(1):109–33.

[30] Rasmussen K J. Full-range stress–strain curves for stainless steel alloys. Journal of Constructional Steel Research 2003;59(1):47–61.

[31] Arrayago I, Real E, Gardner L. Description of stress–strain curves for stainless steel alloys. Materials & Design 2015;87:540–52.

[32] Gardner L, Yun X. Description of stress–strain curves for cold-formed steels. Construction and Building Materials 2018;189:527–38.

[33] Centre for Advanced Structural Engineering, Compression Tests of Stainless Steel Tubular Columns, University of Sydney, Australia; 1990, Investigation report S770.

[34] Gardner L, Nethercot D A. Experiments on stainless steel hollow sections—Part 1: Material and cross-sectional behaviour. Journal of Constructional Steel Research 2004;60(9):1291–318.

[35] dos Santos GB, Gardner L, Kucukler M. A method for the numerical derivation of plastic collapse loads. Thin-Walled Structures 2018;124:258–77.

[36] ABAQUS. ABAQUS/standard user's manual. Version 6.17. Dassault Systemes Simulia Corp. USA; 2017.

[37] Tao Z, Wang ZB, Yu Q. Finite element modelling of concrete-filled steel stub columns under axial compression. Journal of Constructional Steel Research 2013;89:121–31.

[38] Espinos A, Gardner L, Romero ML, Hospitaler A. Fire behaviour of concrete filled elliptical steel columns. Thin-Walled Structures 2011;49(2):239–55.

[39] Wang J, Cheng X, Wu C, Hou C-C. Analytical behavior of dodecagonal concrete-filled double skin tubular (CFDST) columns under axial compression. Journal of Constructional Steel Research 2019;162:105743.

[40] He A, Zhao O. Experimental and numerical investigations of concrete-filled stainless steel tube stub columns under axial partial compression. Journal of Constructional Steel Research 2019;158:405-16.

[41] Cruise RB, Gardner L. Strength enhancements induced during cold forming of stainless steel sections. Journal of Constructional Steel Research 2008;64(11):1310–6.

[42] Wang F. Behaviour and design of concrete-filled double skin stainless steel members. PhD thesis, Department of Civil engineering, the University of Hong Kong, Hong Kong, China; 2018.

[43] Sun Y, Zhao O. Material response and local stability of high-chromium stainless steel welded I-sections. Engineering Structures 2019;178:212–26.

[44] He A, Liang Y, Zhao O. Experimental and numerical studies of austenitic stainless steel CHS stub columns after exposed to elevated temperatures. Journal of Constructional Steel Research. 2019;154:293–305.

[45] Sun Y, Liang Y, Zhao O. Testing, numerical modelling and design of S690 high strength steel welded I-section stub columns. Journal of Constructional Steel Research 2019;159:521–33.

[46] Wang F, Zhao O, Young B. Testing and numerical modelling of S960 ultra-high strength steel angle and channel section stub columns. Engineering Structures 2020; 204:109902.

[47] EN 1993-1-4. Eurocode 3: design of steel structures – Part 1.4: general rules –supplementary rules for stainless steels. Brussels: European Committee for Standardization (CEN); 2006.

[48] Gardner L, Theofanous M. Discrete and continuous treatment of local buckling in stainless steel elements. Journal of Constructional Steel Research 2008;64(11):1207–16.

[49] AS/NZS 4673. Cold-formed stainless steel structures. Sydney: AS/NZS 4673:2001; 2001.

[50] SEI/ASCE 8-02. Specification for the design of cold-formed stainless steel structural members. Reston: American Society of Civil Engineers (ASCE); 2002.

[51] EN 1992-1-1, Eurocode 2: Design of concrete structures-Part 1-1: General rules and rules for buildings, Brussels: European Committee for Standardization (CEN), 2004.

[52] Liew JR, Xiong M, Xiong D. Design of concrete filled tubular beam-columns with high strength steel and concrete. Structures 2016;8;213–226.

[53] Uy B, Bradford M.A. Elastic local buckling of steel plates in composite steel-concrete members. Engineering Structures 1996;18(3):193–200.

[54] Lai Z, Varma AH, Zhang K. Noncompact and slender rectangular CFT members: Experimental database, analysis, design. Journal of Constructional Steel Research 2014;101;455–468.

[55] Leon RT, Kim DK, Hajjar JF. Limit state response of composite columns and beam-columns part 1: Formulation of design provisions for the 2005 AISC specification. Engineering Journal-American Institute of Steel Construction 2007;44(4):341.

Table 1 Measured test specimen dimensions.

Specimen	Length	Outer tube dimensions						Inner tube dimensions			Area: Outer tube	Area: Inner tube	Area: Concrete	Ductility index	Test strengths	P_{FE}/P_{exp}
	L (mm)	D_o (mm)	B_o (mm)	t_o (mm)	D_o/t_o	$r_{int,o}$ (mm)	$r_{ext,o}$ (mm)	D_i (mm)	t_i (mm)	D_i/t_i	A_o (mm^2)	A_i (mm^2)	A_c (mm^2)	DI	P_{exp} (kN)	
AS120×6-HC22×4-C40*	300.0	120.5	120.2	5.95	20.3	5.7	12.4	22.0	4.10	5.4	2617	231	11356	>2.14	2135	0.90
AS120×6-HC22×4-C80	300.0	120.5	120.1	5.98	20.1	5.7	12.4	22.1	4.08	5.4	2629	231	11314	>1.81	2281	0.96
AS120×6-HC22×4-C120	300.0	120.5	120.2	5.92	20.4	5.7	12.4	22.1	4.45	5.0	2604	246	11360	>7.09	2503	0.97
AS120×6-HC22×4-C120R	300.0	120.5	120.2	5.92	20.3	5.7	12.4	22.1	4.29	5.1	2604	240	11355	>3.75	2443	1.00
AS120×6-HC32×6-C40*	300.0	120.5	120.1	5.99	20.1	5.7	12.4	31.9	5.50	5.8	2635	456	10899	>1.01	2348	0.92
AS120×6-HC32×6-C40R	300.0	120.3	120.1	5.94	20.3	5.7	12.4	31.9	5.35	6.0	2610	446	10911	>2.63	2266	0.96
AS120×6-HC32×6-C80	300.0	120.5	120.1	5.95	20.3	5.7	12.4	31.9	5.64	5.7	2614	466	10918	>1.74	2432	0.93
AS120×6-HC32×6-C120	300.0	120.5	120.5	5.92	20.3	5.7	12.4	32.1	5.74	5.6	2609	475	10963	>2.96	2584	0.96
AS120×6-HC32×6-C120R	300.0	120.4	120.5	5.93	20.3	5.7	12.4	32.0	5.69	5.6	2609	471	10956	>6.76	2643	0.98
AS150×3-HC22×4-C40	375.0	150.8	150.4	2.80	53.8	5.8	8.0	22.0	4.11	5.4	1630	231	20600	4.77	1566	0.98
AS150×3-HC22×4-C40R	375.0	150.6	150.2	2.82	53.5	5.8	8.0	22.1	4.10	5.4	1635	232	20534	2.01	1592	0.96
AS150×3-HC22×4-C80	375.0	150.7	150.1	2.80	53.8	5.8	8.0	22.2	4.08	5.4	1627	232	20563	1.23	2465	0.96
AS150×3-HC22×4-C120	375.0	150.8	150.2	2.82	53.5	5.8	8.0	22.1	4.07	5.4	1638	230	20564	1.13	3258	0.92
AS150×3-HC32×6-C40	375.0	150.9	150.1	2.81	53.6	5.8	8.0	31.9	5.42	5.9	1635	451	20148	>4.74	1695	0.96
AS150×3-HC32×6-C80	375.0	150.7	150.0	2.79	53.9	5.8	8.0	32.0	5.47	5.8	1623	455	20125	1.27	2482	0.98
AS150×3-HC32×6-C120	375.0	150.7	150.1	2.81	53.6	5.8	8.0	31.9	5.57	5.7	1635	462	20137	1.07	3275	0.94
AS150×3-HC89×4-C40	375.0	151.0	150.1	2.75	55.0	5.8	8.0	89.0	3.89	22.9	1596	1040	14780	1.54	2034	0.94
AS150×3-HC89×4-C80	375.0	151.2	150.0	2.76	54.8	5.8	8.0	88.9	3.89	22.9	1605	1039	14808	1.15	2243	1.08
AS150×3-HC89×4-C120	375.0	151.1	150.6	2.75	55.1	5.8	8.0	89.0	3.92	22.7	1600	1047	14882	1.10	3043	0.96
Mean																0.96
COV																0.038

Note: * Ultimate load was determined as the load where the slope of the load-average axial strain curve reached 1% of its initial stiffness.

Table 2 Measured material properties obtained from tensile coupon tests.

Section	$\sigma_{0.2}$ (MPa)	σ_u (MPa)	E (GPa)	ε_f (%)	n	m	$\sigma_u/\sigma_{0.2}$
AS120×3-F	287	645	205	67	4	3	2.4
AS120×6-C	565	779	187	55	3	4	1.4
AS150×3-F	273	754	204	50	4	2	2.8
AS150×3-C	518	882	193	40	4	3	1.7
HC22×4	794	901	197	5	6	4	1.1
HC32×6	619	811	208	9	5	4	1.3
HC89×4	1029	1093	209	6	6	4	1.1

Table 3 Concrete mix design.

Nominal concrete strength (MPa)	Mix proportions (to the weight of cement)					
	Cement	Water	Fine aggregate	10 mm aggregate	CSF[a]	SP[b]
C40	1	0.56	1.67	2.51	0	0.004
C80	1	0.32	1.25	1.88	0	0.020
C120	1	0.21	1.02	1.53	0.09	0.053

Note: [a]CSF = Condensed silica fume; [b]SP = Super plasticizer

Table 4 Measured concrete cylinder strengths.

	Mean value of concrete strength 28-day (MPa)	Coefficient of variation (COV)	Number of concrete cylinder tests	Mean value of concrete strength at days of column tests (MPa)	Coefficient of variation (COV)	Number of concrete cylinder tests
C40	36.2	0.031	4	40.5	0.026	5
C80	77.6	0.028	4	79.9	0.040	7
C120	108.2	0.080	4	115.6	0.025	6

Table 5 Ranges of variation of parameters for the parametric study.

Parameter		d_o/t_o	D_i/t_i	f_c (MPa)
Range	Max.	146	200	120
	Min.	6	5	40

Table 6. Limitations on cross-sectional slendernesses and material strengths in design codes.

Design codes	Limitations of cross-sectional slenderness: Original	Limitations of cross-sectional slenderness: Normalised slenderness limits	$\sigma_{0.2}$ (MPa)	f_c (MPa)
EN 1994-1-1	$D_o/t_o \leq 52\sqrt{\frac{235}{\sigma_{0.2,o}}\frac{E_o}{210000}}$	$(D_o/t_o)\sqrt{\frac{210000}{E_o}\frac{\sigma_{0.2,o}}{235}} \leq 52$	235-460	20-50
AS 5100	$\lambda_e = \frac{d_o}{t_o}\sqrt{\frac{\sigma_{0.2,o}}{235}} \leq 40$	$\frac{d_o}{t_o}\sqrt{\frac{\sigma_{0.2,o}}{235}} \leq 40$	230-400	25-65
AISC 360	$\lambda_p = \frac{d_o}{t_o} \leq 2.26\sqrt{\frac{E_o}{\sigma_{0.2,o}}}$	$(d_o/t_o)\sqrt{\frac{\sigma_{0.2,o}}{E_o}} \leq 2.26$	≤ 525	21-70
ACI 318	$t_o \geq D_o\sqrt{\frac{\sigma_{0.2,o}}{3E_o}}$	$(D_o/t_o)\sqrt{\frac{\sigma_{0.2,o}}{E_o}} \leq \sqrt{3}$	≤ 345	≥ 17.2

Table 7 Comparison of stub column test and FE results with predicted strengths.

No. of tests: 19 No. of FE simulations: 290		EC4	EC4#	AS 5100	AS 5100#	AISC 360	AISC 360#	ACI 318	ACI 318#
P_u/P_{code}	Mean	1.14	1.16	1.11	1.13	1.28	1.30	1.27	1.30
	COV	0.211	0.209	0.227	0.225	0.182	0.180	0.173	0.173

Note: # Predicted strength considering effective area of inner tube.

Table 8 Test and FE strengths and design predictions with the inclusion of η for specimens falling within their respective codified slenderness limits.

f_c		Ratio of test-to-predicted strengths							
(MPa)		P_u/P_{EC4}	P_u/P_{EC4*}	P_u/P_{AS5100}	$P_u/P_{AS5100*}$	P_u/P_{AISC}	P_u/P_{AISC*}	P_u/P_{ACI}	P_u/P_{ACI*}
40	Mean	1.43	1.43	1.47	1.47	1.42	1.42	1.53	1.53
	COV	0.257	0.257	0.249	0.249	0.251	0.251	0.232	0.232
80	Mean	1.12	1.22	1.16	1.25	1.20	1.30	1.25	1.34
	COV	0.057	0.056	0.043	0.049	0.061	0.062	0.049	0.056
120	Mean	1.08	1.23	1.10	1.24	1.18	1.34	1.21	1.35
	COV	0.035	0.040	0.021	0.033	0.047	0.058	0.029	0.042
Sum	Mean	1.30	1.35	1.37	1.41	1.34	1.38	1.44	1.48
	COV	0.251	0.222	0.251	0.230	0.229	0.209	0.230	0.212

Note: * Modified predicted strength incorporating effective compressive strength of concrete.

Table 9 Test and FE strengths and design predictions incorporating k=4 and k=10.67 for specimens exceeding their respective codified slenderness limits.

CFDST		Ratio of test-to-predicted strengths					
Test + FE		P_u/P_{EC4}	$P_u/P_{EC4\wedge}$	P_u/P_{AS5100}	$P_u/P_{AS5100\wedge}$	P_u/P_{ACI}	$P_u/P_{ACI\wedge}$
SHS-CHS	Mean	1.04	1.02	1.08	1.03	1.20	1.15
	COV	0.048	0.038	0.053	0.037	0.066	0.055

Note: ^ Modified predicted strength incorporating a higher buckling coefficient k=10.67.

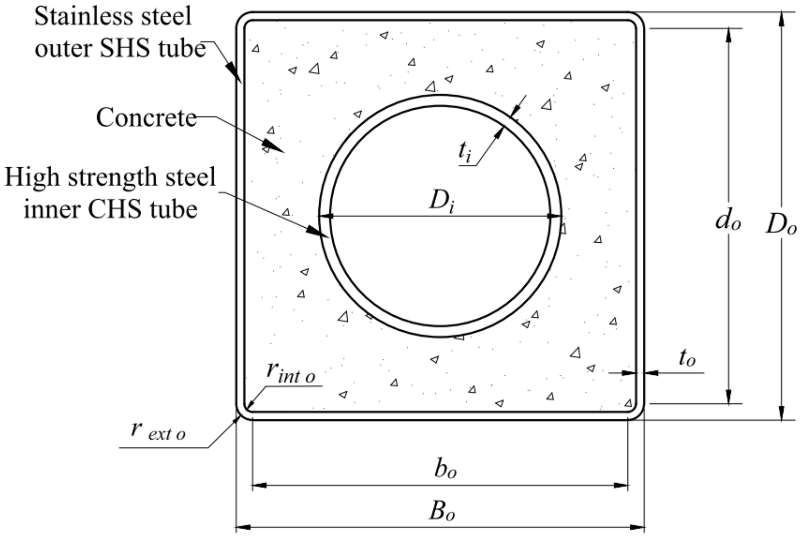

Fig. 1. Definition of symbols for CFDST specimens

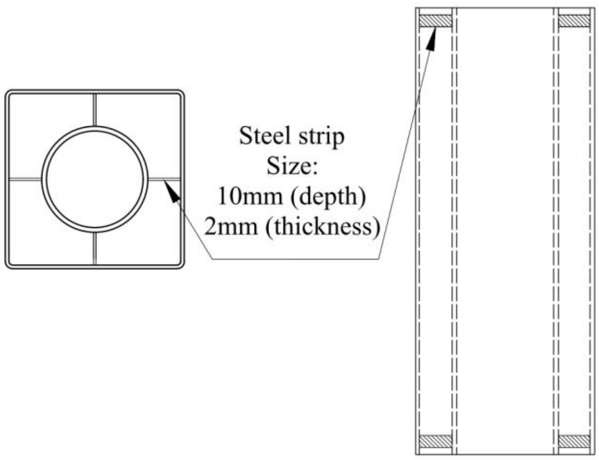

Fig. 2. Fabrication of the tubes prior to casting

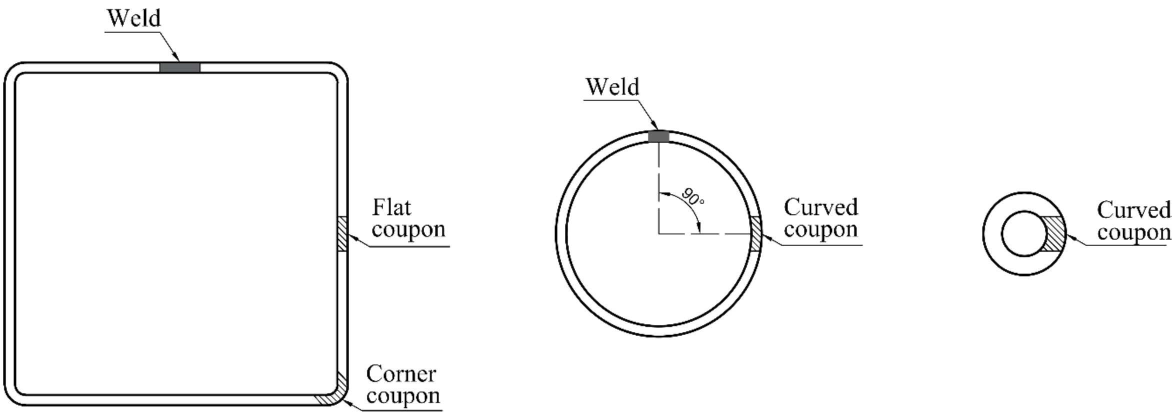

(a) SHS outer tube

(b) CHS inner tubes

Fig. 3. Locations of tensile coupons within the cross-sections

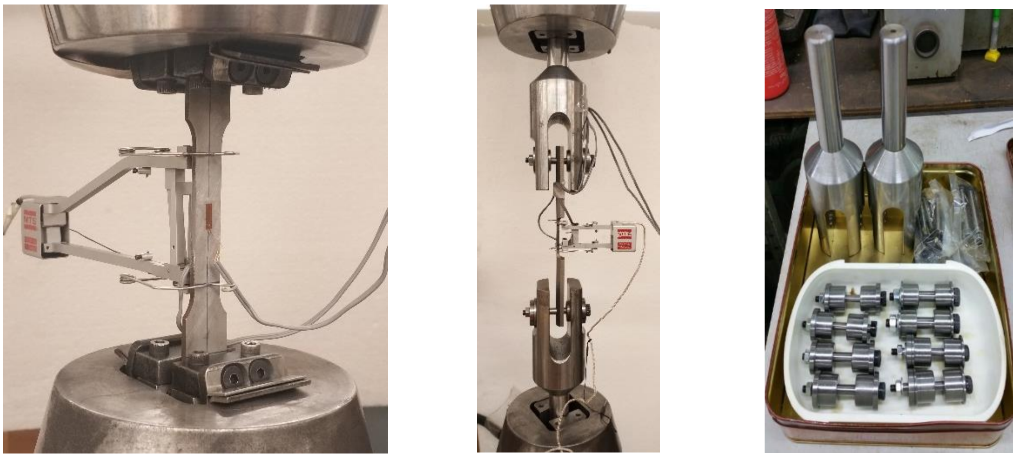

(a) (b) (c)

Fig. 4. Longitudinal tensile coupon tests, showing (a) flat coupon test arrangement (b) corner or curved coupon test arrangement (c) accessories for corner or curved coupon test setup.

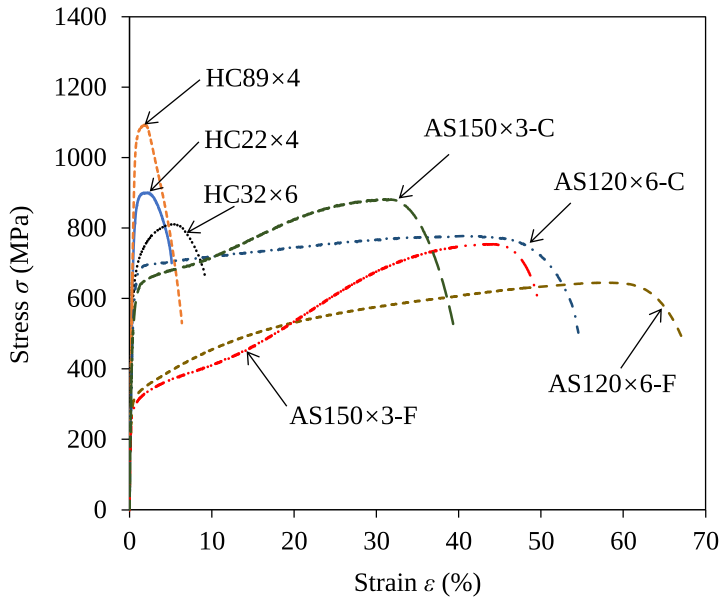

Fig. 5. Full stress–strain curves obtained from longitudinal tensile coupon tests.

(a) Experimental setup

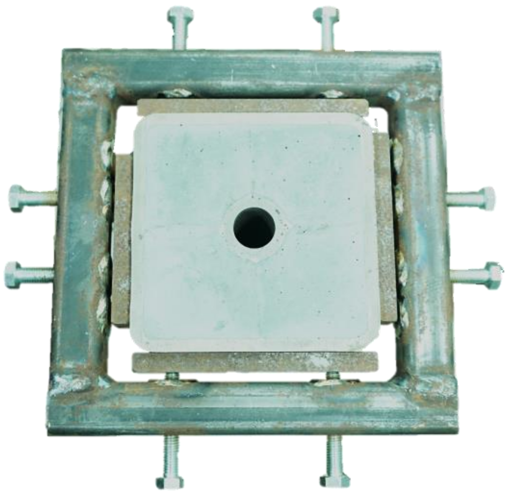

(b) Special clamping device

Fig. 6. Test set-up for CFDST stub column specimens.

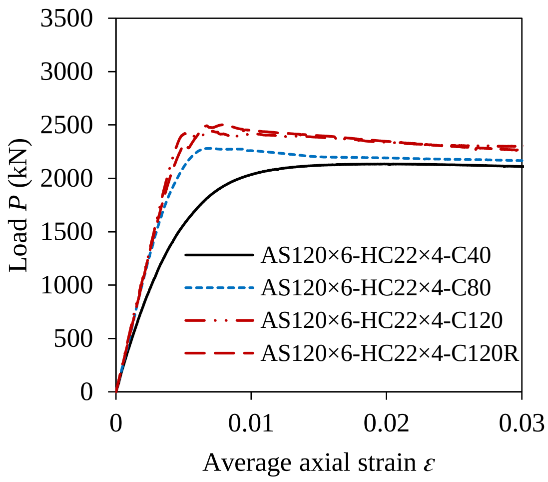

(a) AS120×6-HC22×4

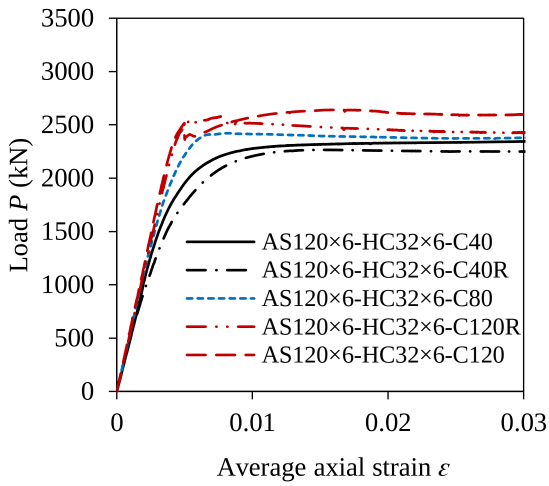

(b) AS120×6-HC32×6

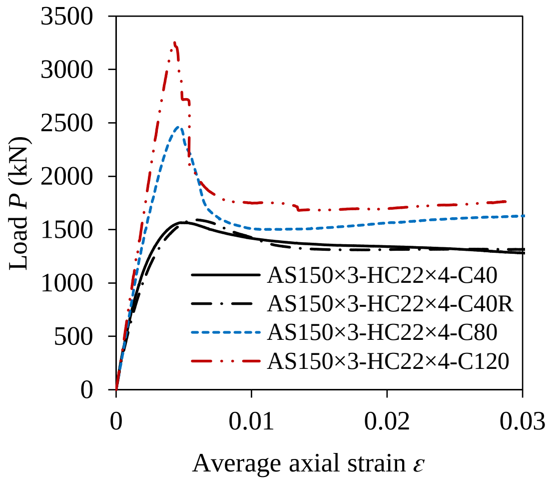

(c) AS150×3-HC22×4

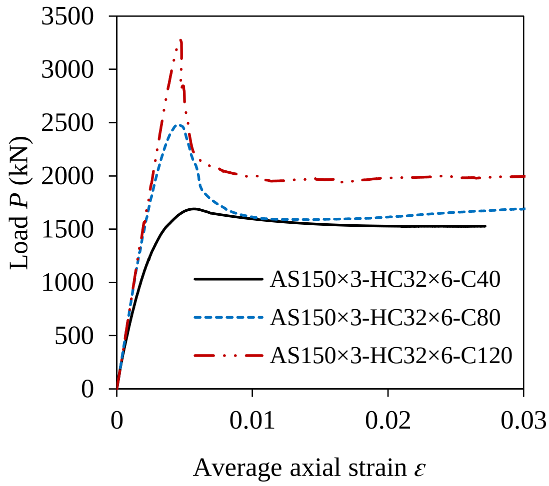

(d) AS150×3-HC32×6

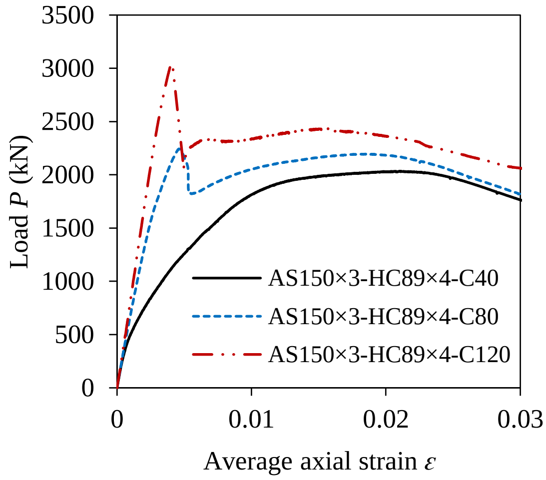

(e) AS150×3-HC89×4

Fig. 7. Load-average axial strain curves for tested CFDST stub columns.

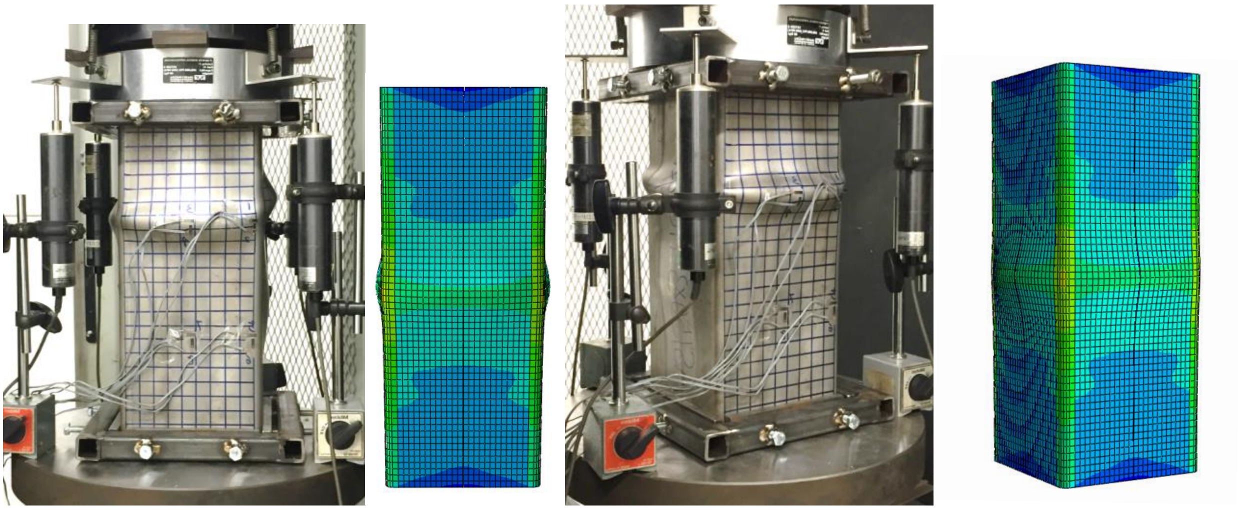

(a) Front view

(b) Side view

Fig. 8. Experimental and numerical failure modes of stub columns (AS150×3-HC89×4-C80)

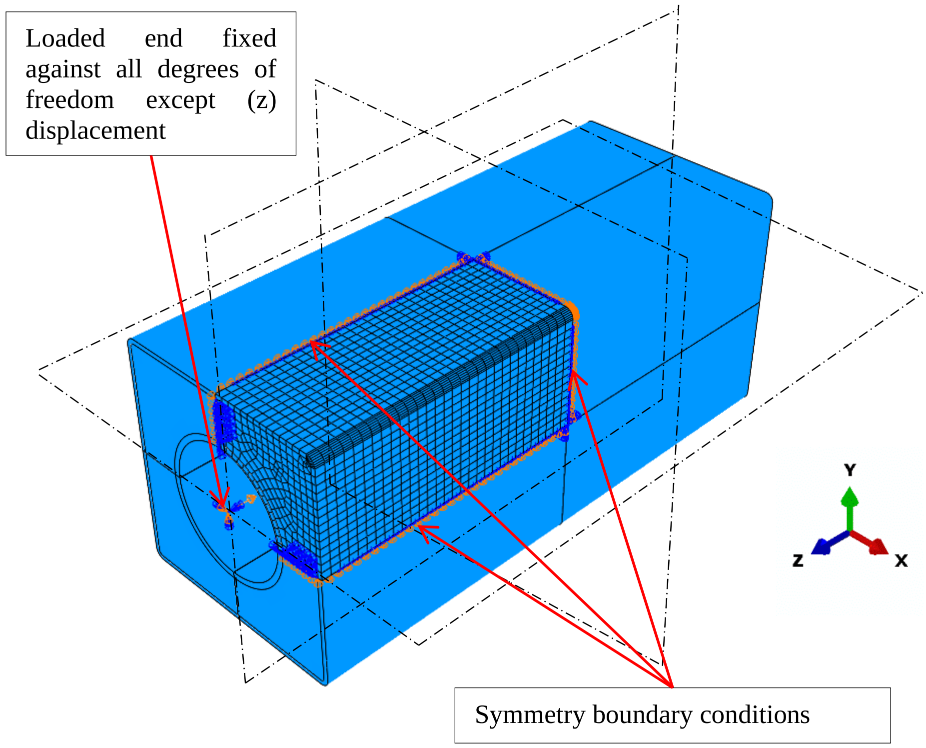

Fig. 9. Stub column FE model in ABAQUS.

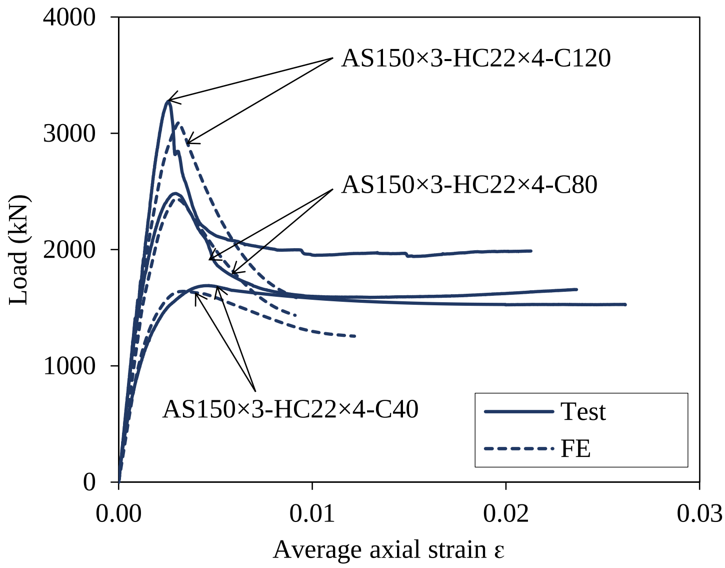

Fig. 10. Comparisons of test and FE load-average axial strain curves.

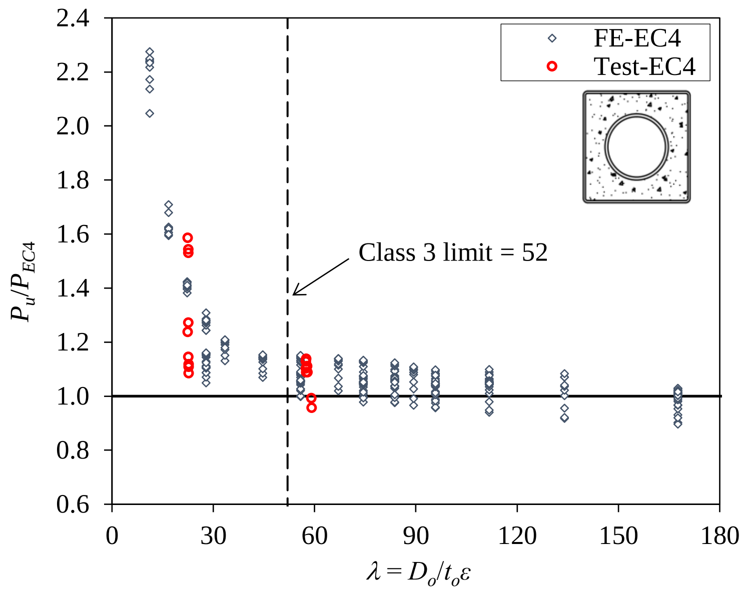

Fig. 11. Comparison of test and FE results with strength predictions from EC4.

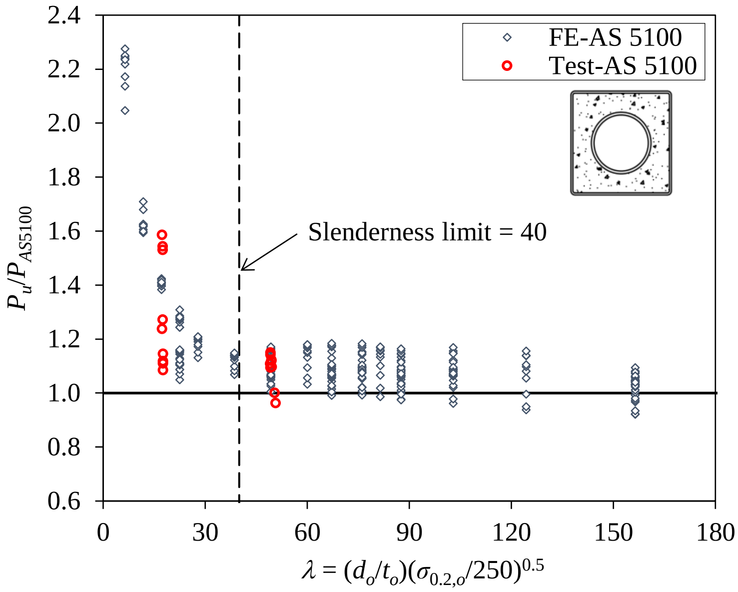

Fig. 12. Comparison of test and FE results with modified strength predictions from AS 5100.

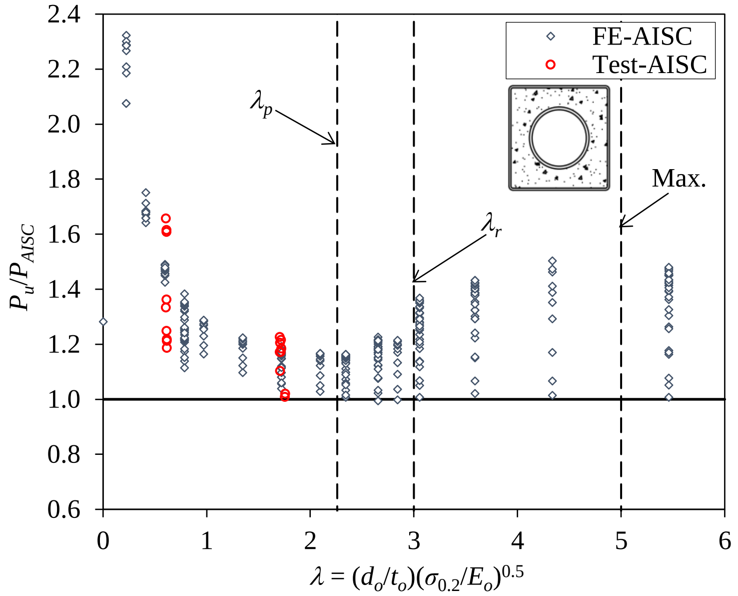

Fig. 13. Comparison of test and FE results with modified strength predictions from AISC 360.

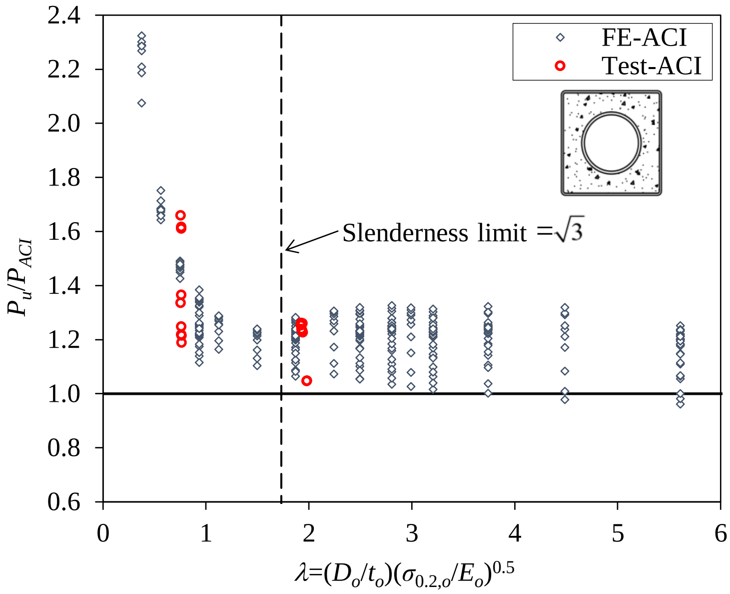

Fig. 14. Comparison of test and FE results with modified strength predictions from ACI 318.